Progress In Electromagnetics Research C, Vol. 160, 94–103, 2025

PIER C

(Received 8 June 2025, Accepted 16 September 2025, Scheduled 25 September 2025)

Design and Optimization of the PMDCM with Concave Slots Halbach Array Magnetic Ring

Chengcheng Zeng and Quanfeng Li*

School of Electrical Engineering, Shanghai DianJi University, Shanghai 201306, China

ABSTRACT: The permanent magnet brushed DC motor (PMDCM) features a simple structure and reliable performance, making it widely used in home appliances and automotive applications. To further optimize the output torque quality of the PMDCM, this paper proposes a concave-slot Halbach array magnet ring (CSHAMR) structure. First, a finite element model was established to analyze the electromagnetic characteristics of the motor. By comparing with the traditional Halbach array magnetic ring (THAMR), the superiority of the proposed structure for the application in brushed motors was verified. Secondly, by defining the magnitude of the no-load back electromotive force (EMF) generated by a unilateral conductor within the interval γ, the optimization level of the CSHAMR structure for commutation performance was evaluated. The influence of concave slot parameters on motor commutation performance under different values was analyzed. Finally, a parametric model of the CSHAMR was established, and multi-objective optimization of the motor was performed based on the particle swarm optimization (PSO) algorithm. The results demonstrate that CSHAMR can effectively reduce torque ripple and cogging torque in PMDCM motors while improving motor commutation performance.

1. INTRODUCTION

Permanent magnet brushed DC motors (PMDCMs) have a relatively simple overall control circuit compared to brushless DC motor, which does not require a controller and can be started or braked by electrifying the motor [1]. However, the unique structure of permanent magnet motors leads to cogging torque and torque ripple, causing motor vibration and noise, increasing the motor's starting resistance torque and affecting the quality of the motor's output torque [2, 3]. Furthermore, the quality of commutation performance in PMDCM directly impacts its service life. Consequently, optimizing motor output torque quality and improving commutation performance have become key challenges for PMDCM.

Through in-depth research on permanent magnet materials and structures, Halbach discovered the Halbach permanent magnet array (HPMA) structure in 1979 while conducting electron acceleration experiments [4]. This structure represents an engineering approximation of an ideal configuration, capable of generating the strongest magnetic field using the minimum number of magnets. Since the 1990s, an increasing number of scholars have begun applying HPMA structures to the field of electric motors, achieving significant research results [5–8]. Different HPMA structures can be applied to different types of motors. For instance, linear HPMA structures are primarily used in linear motors, while ring-type HPMA structures are mainly applied in rotating motors.

HPMA structure can alter the air-gap magnetic field distribution of the motor, thereby optimizing the quality of the motor's output torque [9, 10]. Tymosch et al. [11] investigated the application of Halbach arrays in superconducting permanent magnet synchronous motors, and the final results showed that Halbach arrays significantly enhanced the motor magnetic field strength and increased the motor power density. Shen and Zhu [12] proposed a T-type array as an alternative to the conventional three-segment HPMA. This structure holds the potential to simultaneously achieve low torque ripple and high electromagnetic torque in electric motors. In [13–15], a novel double-layer HPMA structure was applied to multiple motors with different configurations. By optimizing the angle ratio and height between the two layers, the motors achieved a more sinusoidal electromotive force and reduced torque ripple. Zhang et al. [16] proposed a trapezoidal HPMA structure with radially infinite layering, treating each layer as a conventional HPMA. They ultimately derived an analytical magnetic field model through magnetic field superposition. Shi et al. [17] proposed analytical magnetic field models for cylindrical HPMA structures, which can intuitively illustrate the relationship between relevant motor design parameters and air-gap magnetic flux density.

Some scholars have also combined HPMA structure with optimization algorithms to perform multi-objective optimization design on electric motors. In [18] by Lv et al., a three-stage nonuniform Halbach magnetization in the form of an external rotor permanent magnet synchronous motor is optimized, and various electromagnetic properties of the motor are significantly improved after the optimization. In [19] by Li et al., Halbach eccentric poles are used to study the effect of pole-related structural parameters on the performance of the motor, and base NSGA-II algorithm is used for the multi-objective optimization of the motor. All the performances of the optimized motor are better than the prototype.

---

* Corresponding author: Quanfeng Li (lqf108359@163.com).

doi:10.2528/PIERC25060803

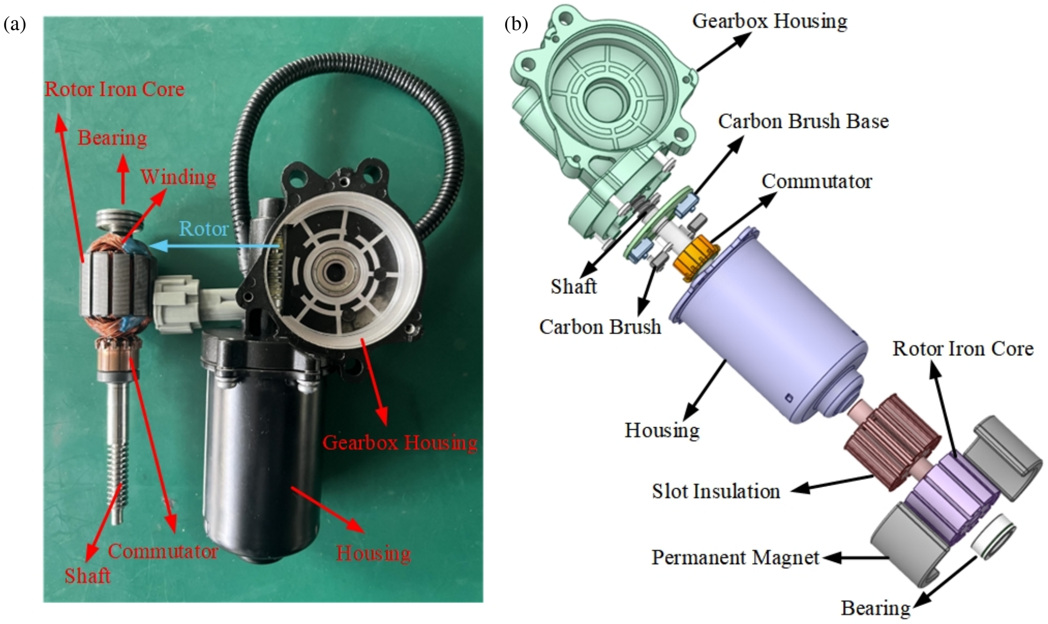

FIGURE 1. Motor structure schematic: (a) The prototype physical picture; (b) Exploded view of the prototype structure.

TABLE 1. Main performance parameters of the prototype.

Parameters	Unit	Value
Rated voltage	V	12
Rated speed	rpm	1505
Rated torque	mN·m	263.5
No-load speed	rpm	3200
Rated current	A	9.2
No-load current	A	0.8

Current research on the application of HPMA structures in electric motors has primarily focused on brushless motors or permanent magnet synchronous motors, with relatively few studies exploring their use in brushed motors. Although the HPMA structure generates an ideal sinusoidal air-gap magnetic field that effectively reduces cogging torque and torque ripple, this sinusoidal field may simultaneously increase magnetic flux density within the commutation interval, leading to degraded commutation performance in the motor.

To conduct in-depth research on the application of HPMA in brushed motors, this paper proposes a CSHAMR structure featuring concave slots on both sides using a 2-pole, 12-slot PMDCM as an example. This design addresses the degradation of motor commutation performance caused by THAMR. The optimization level of commutation performance is evaluated by defining the magnitude of the no-load counter-electromotive force generated by the unilateral conductor within the interval γ in the winding. Multi-objective optimization design of the motor is achieved by incorporating the concave slot parameters in the CSHAMR structure as optimization variables and applying the PSO algorithm.

TABLE 2. Main size parameters of the prototype.

Parameters	Unit	Value
Iron core outer diameter	mm	35.6
Iron core inner diameter	mm	10
Iron core stack thickness	mm	27.5
Magnet outer diameter	mm	48
Magnet inner diameter	mm	36.6
Pole embrace		0.72
Magnet length	mm	33
Outer diameter of housing	mm	53
Air-gap length	mm	0.5

2. MODEL BUILDING AND CONCAVE SLOTS DESIGN

2.1. Motor Structure and Main Performance Parameters

In this paper, a 2-pole, 12-slot PMDCM is optimized. The structure of the motor is shown in Figure 1, and the main performance parameters are shown in Table 1. The size parameters are shown in Table 2.

2.2. Modeling and Magnetic Field Analysis of the THAMR

The most basic Halbach array consists of an array of permanent magnets with radial magnetization and tangential magnetization arranged together to achieve magnetic field concentration on one side.

The relationship between the magnetization angle θ_m and magnetization position angle θ_k of the magnet in polar coordinates for an ideal Halbach array is shown in Figure 2, where the mathematical model of the magnetization vector $\mathbf{M}$ in polar coordinates [20] can be expressed by formulas (1) and (2). At

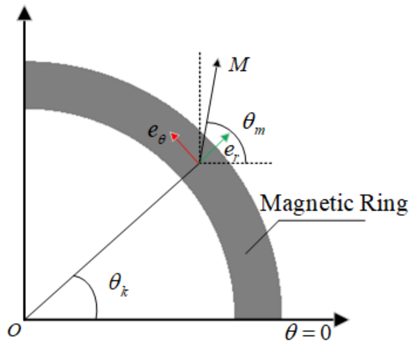

FIGURE 2. The Halbach array magnetization angle versus magnetization position.

this point, θ_k can be viewed as a continuous function.

$$\theta_m = (1 \pm p)\,\theta_k \tag{1}$$

$$\mathbf{M} = M_0 \cos(p\theta_k)\,\mathbf{e_r} \mp M_0 \sin(p\theta_k)\,\mathbf{e}_\theta \tag{2}$$

where $\mathbf{e_r}$, $\mathbf{e}_\theta$ are radial and tangential unit vectors, respectively; M_0 is the magnetization strength, which is numerically equal to the ratio of the material remanent magnetization and the relative permeability; and p denotes the pole pair number. The "−", "+" in formula (2) indicate that the magnetic field gathers outward or inward, respectively

For THAMR, the magnetization position angle θ_k can be determined by the center position of each permanent magnet, in which θ_k can be expressed by the following formula (3) [17]:

$$\theta_k = \frac{k-1}{pl}\pi \tag{3}$$

where l denotes the number of chunks per pole of the magnetic ring, and $k = 1, 2, 3, \ldots, 2pl$ denotes the kth permanent magnet. Shi et al. [17] developed the derivation of the air-gap magnetic field model for inward and outward aggregation of the magnetic field after using the THAMR, respectively, while neglecting the motor tooth slot effect, in which the derivation process for the inward aggregation of the magnetic field can be roughly summarized as follows.

In $[-\pi/p, \pi/p]$, the radial component M_r and tangential component M_0 of the magnetization intensity vector $\mathbf{M}$ can be expanded in the Fourier series with the expressions shown in formulas (4)–(6), where $i = 1, 2, 3, \ldots$.

When $np \neq 1$

$$M_{rn} = \begin{cases} \frac{2pl}{\pi} M_0 \sin\left(\frac{1+p}{2pl}\pi\right) \frac{(-1)^{\frac{n-1}{2l}}}{np+1} & n = 2li+1 \\ -\frac{2pl}{\pi} M_0 \sin\left(\frac{1+p}{2pl}\pi\right) \frac{(-1)^{\frac{n+1}{2l}}}{np-1} & n = 2li-1 \\ 0 \quad \text{others} \end{cases} \tag{4}$$

$$M_{\theta n} = \begin{cases} \frac{2pl}{\pi} M_0 \sin\left(\frac{1+p}{2pl}\pi\right) \frac{(-1)^{\frac{n-1}{2l}}}{np+1} & n = 2li+1 \\ \frac{2pl}{\pi} M_0 \sin\left(\frac{1+p}{2pl}\pi\right) \frac{(-1)^{\frac{n+1}{2l}}}{np-1} & n = 2li-1 \\ 0 \quad \text{others} \end{cases} \tag{5}$$

When $np = 1$

$$M_{r1} = M_{\theta 1} = M_0 \frac{\sin\frac{\pi}{l}}{\frac{\pi}{l}} \tag{6}$$

Using the magnetic scalar potential φ, combined with the magnetization characteristics in regions I and II (as shown in Figure 3), the control equations and corresponding boundary conditions for the two regions can be listed. Finally, according to $\mathbf{H} = -grad\varphi$, the air gap magnetic density in Region II can be expression by formulas (7)–(11).

When $np \neq 1$

$$B_{2r}(r,\theta) = -\sum_n G \times \left[\left(\frac{r}{R_{mi}}\right)^{np-1} + \left(\frac{R_i}{R_{mi}}\right)^{np-1} \left(\frac{R_i}{r}\right)^{np+1}\right] \times \cos(np\theta) \tag{7}$$

$$B_{2\theta}(r,\theta) = \sum_n G \times \left[\left(\frac{r}{R_{mi}}\right)^{np-1} - \left(\frac{R_i}{R_{mi}}\right)^{np-1} \left(\frac{R_i}{r}\right)^{np+1}\right] \times \sin(np\theta) \tag{8}$$

$$G = \frac{\mu_0 np \left\{ \begin{array}{c} \frac{M_{rn}+M_{\theta n}}{np-1} - \frac{M_{rn}-M_{\theta n}}{np+1}\left(\frac{R_{mi}}{R_{mo}}\right)^{2np} \\ -\frac{2(M_{rn}+npM_{\theta n})}{(np)^2-1}\left(\frac{R_{mi}}{R_{mo}}\right)^{np-1} \end{array} \right\}}{\left\{ \begin{array}{c} \left[(\mu_r+1)\left(\frac{R_i}{R_{mo}}\right)^{2np} - (\mu_r-1)\left(\frac{R_{mi}}{R_{mo}}\right)^{2np}\right] \\ -\left[\left((\mu_r+1) - (\mu_r-1)\left(\frac{R_i}{R_{mi}}\right)^{2np}\right)\right] \end{array} \right\}} \tag{9}$$

When $np = 1$

$$B_{2r}(r,\theta) = -G \times \left[1 + \left(\frac{R_i}{r}\right)^2\right] \cos(\theta) \tag{10}$$

$$B_{2\theta}(r,\theta) = G \times \left[1 - \left(\frac{R_i}{r}\right)^2\right] \sin(\theta) \tag{11}$$

$$G = \frac{\mu_0 \left\{ \begin{array}{c} \frac{M_{r1}-M_{\theta 1}}{2}\left[1 - \left(\frac{R_{mi}}{R_{mo}}\right)^2\right] \\ -(M_{r1} + M_{\theta 1}) \ln\left(\frac{R_{mi}}{R_{mo}}\right) \end{array} \right\}}{\left\{ \begin{array}{c} \left[(\mu_r+1)\left(\frac{R_i}{R_{mo}}\right)^2 - (\mu_r-1)\left(\frac{R_{mi}}{R_{mo}}\right)^2\right] \\ -\left[\left((\mu_r+1) - (\mu_r-1)\left(\frac{R_i}{R_{mi}}\right)^2\right)\right] \end{array} \right\}} \tag{12}$$

To facilitate the numerical calculation, the coefficient G in formulas (7), (8), (10), and (11) can be expressed by formulas (9) and (12), where the positional relationships of R_i, R_{mo}, and R_{mi} are shown in Figure 3. μ_0 is the vacuum permeability, and μ_r is the relative remanent permeability of the permanent magnet.

The magnetization method of 10 pieces per pole will be adopted in this paper, and the material (ferrite) and magnetic field gathering direction of the THAMR are the same as that of the prototype. The magnetization direction of each piece of permanent magnet can be calculated from formulas (2) and (3), and the results are shown as indicated by the red arrows in Figure 3.

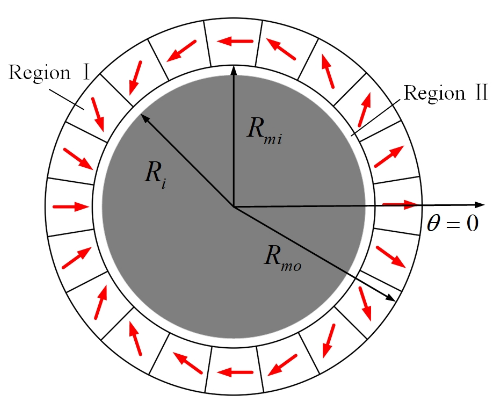

FIGURE 3. Direction of the magnetization of each permanent magnet.

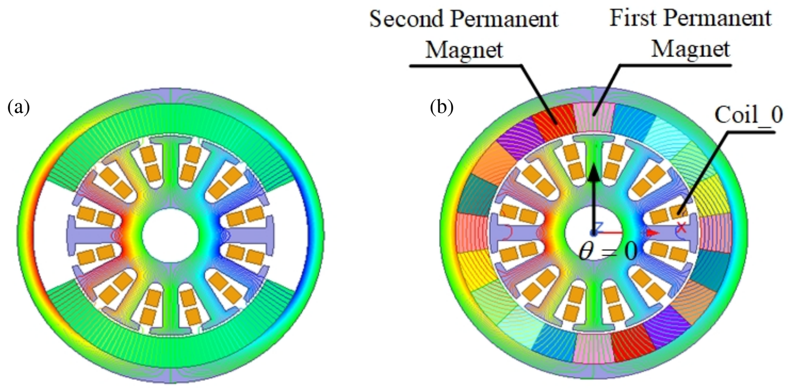

FIGURE 4. Distribution of the magnetic lines: (a) The prototype; (b) The THAMR.

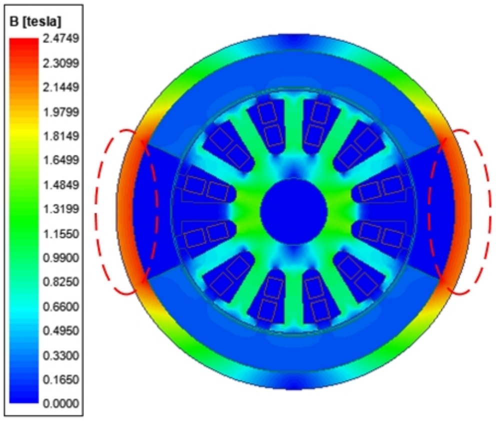

FIGURE 5. The magnetic flux density distribution of the prototype.

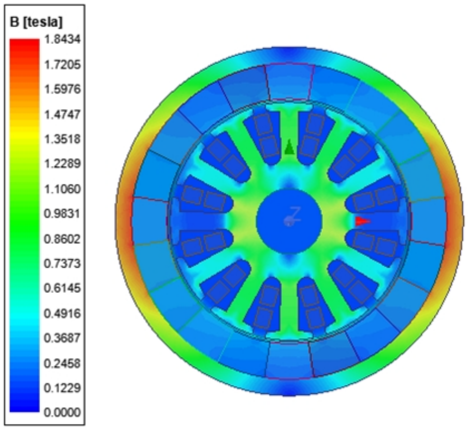

FIGURE 6. The magnetic flux density distribution of the THAMR scheme.

2.3. PMDCM Simulation Model Building and Analysis

The pair of magnetic poles in the prototype is distributed up and down in Maxwell 2D, as shown in Figure 4(a). To ensure the same phase of the initial magnetic field with the prototype, THAMR magnetization method should be selected as column coordinate magnetization, and a new reference coordinate system needs to be established, as shown in Figure 4(b). The distribution of magnetic lines of the prototype model and the THAMR scheme model is shown in Figure 4.

As can be seen in Figure 4, most of the magnetic lines of force are closed along the permanent magnets, machine housing, airgap, and rotor core. Due to the difference in the structure of permanent magnets, the direction of the magnetic lines of force on the left and right sides of the motor is slightly different between the prototype and THAMR scheme, and as a result, there will be a difference in the magnetic flux density distribution between the two schemes. The magnetic flux density distributions for the prototype and THAMR scheme are shown in Figure 5 and Figure 6.

The highest magnetic density of the machine housing can be seen in the magnetic flux density cloud diagram. Since the permanent magnets in the prototype are of a tile-shaped structure, there are no permanent magnets inside the machine housing between the two magnetic poles (as shown in the red circle in Figure 5). Therefore, the magnetic flux density in this area is largely dependent on the thickness of the machine housing. If a thinner machine housing is used, it may lead to local magnetic saturation issues. After using THAMR, due to the magnetic ring structure, some of the magnetic lines of force can be directly closed through the magnetic ring. Compared with the prototype, this can effectively reduce the magnetic flux density on both sides of the machine housing, thereby improving the local magnetic saturation problem.

Figure 7 shows the results of radial air-gap magnetic flux density calculations for the positive half-axis of the motor distributed along the circumference of the motor under the action of a static magnetic field, which is an approximate trapezoidal wave for the prototype and an approximate sinusoidal wave for the THAMR. Figure 8 shows the results of fast Fourier transform (FFT) calculations of the radial air-gap magnetic flux density, and then combined with formula (13), the total harmonic distortion rate (THD) of the radial air-gap magnetic density can be obtained.

$$\mathrm{THD} = \frac{\sqrt{B_{r2}^2 + B_{r3}^2 + \cdots + B_{rk}^2}}{B_{r1}} \times 100\% \tag{13}$$

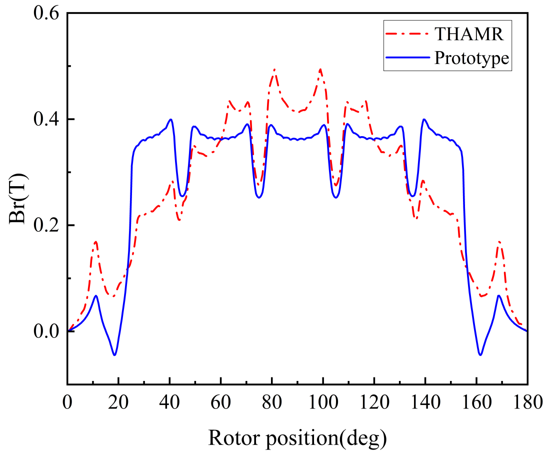

FIGURE 7. The radial air-gap magnetic flux density waveforms of the prototype and THAMR.

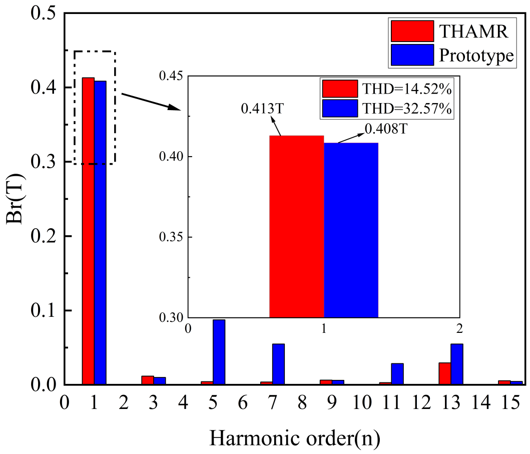

FIGURE 8. The FFT calculations of the radial air-gap magnetic flux density.

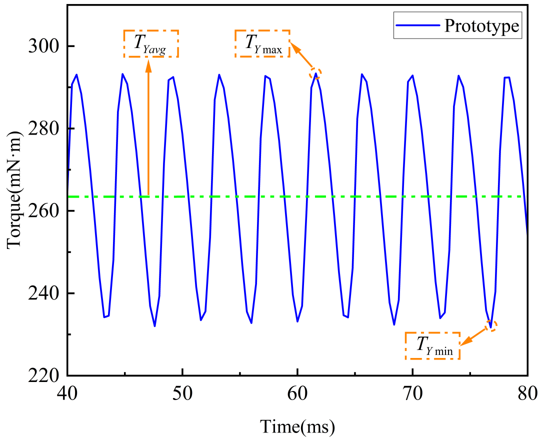

FIGURE 9. The torque curves of the prototype.

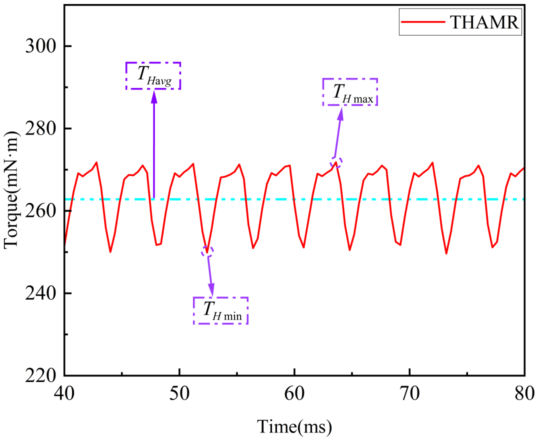

FIGURE 10. The torque curves of the THAMR.

where B_{rk} $(k = 2, 3, \ldots)$ is the kth amplitude of the radial air-gap magnetic density, and B_{r1} is the radial air-gap magnetic density fundamental wave amplitude.

It can be seen that the THD of the radial air-gap magnetic density after using the THAMR is 14.52%, which is lower than that of the prototype. Its fundamental wave amplitude is 0.413 T, which is higher than the 0.408 T of the prototype. The 5th and 7th harmonics are also significantly reduced compared to the prototype.

The torque ripple of the motor has a large impact on both the stability and service life of the motor, and the motor torque ripple T_r is calculated by formula (14).

$$T_r = \frac{T_{\max} - T_{\min}}{T_{avg}} \times 100\% \tag{14}$$

where T_r is the torque ripple; $T_{\max}$ is the maximum value of torque; $T_{\min}$ is the minimum value of torque; T_{avg} is the average value of torque. When the motor operates stably under rated conditions, the torque curves for the prototype and THAMR are shown in Figure 9 and Figure 10.

In Figure 9, $T_{Y\max}$, $T_{Y\min}$, T_{Yavg}, and T_{Yr} represent the torque maximum, torque minimum, torque average, and torque ripple of the prototype, respectively. In Figure 10, $T_{H\max}$, $T_{H\min}$, T_{Havg}, and T_{Hr} represent the torque maximum, torque minimum, torque average, and torque ripple of the THAMR, respectively. The average torque of the prototype is 263.5 mN·m, while that of the THAMR is 262.8 mN·m.

According to formula (14), the torque ripple of the prototype is 23.12% while that of the THAMR is 8.27%. The results show that after using THAMR in this paper, the average value of the motor's torque decreases slightly compared to the prototype, but the optimization of the motor's torque ripple is more obvious.

2.4. Design of the CSHAMR

Brushed DC motors generate electric sparks during commutation due to their unique mechanical commutation structure. To reduce the electric spark, the magnetic field within the commutation interval should be required to be as small as possible to reduce the armature reaction potential of the commutation element [21]. The approximate sinusoidal air-gap magnetic field generated by the use of the THAMR has a high magnetic field strength in the commutation interval of the motor, which is not

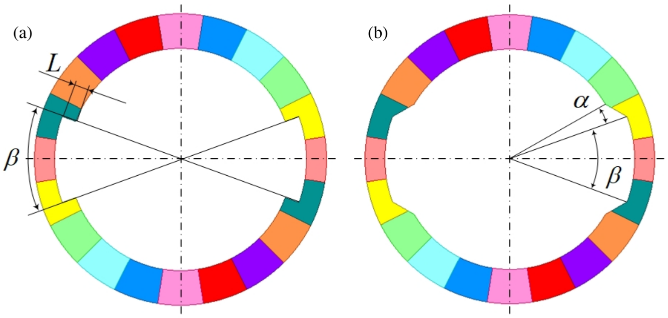

FIGURE 11. The schematic structure of the CSHAMR: (a) $\alpha = 0°$; (b) $\alpha \neq 0°$.

conducive to motor commutation. In this paper, the magnetic field strength in the commutation interval will be reduced by opening concave slots on both sides of the THAMR. The structure of the CSHAMR is shown in Figure 11, where L, β, and α denote the depth of the concave slots, arc angle, and edge transition angle, respectively. When the tooth slot effect is neglected, the no-load back EMF waveform of the unilateral conductor Coil_0 (shown in Figure 4b) depends entirely on the air-gap magnetic field waveform, and the commutation interval of Coil_0 is located near the electrical angle of $165° \pm 15$.

Considering that the armature reaction of the motor can lead to distortions in the air-gap magnetic field, causing a magnetic field zero shift, the range of intervals of concern should be slightly larger than the commutation intervals. In this paper, focus is on the no-load back EMF magnitude F of the unilateral conductor Coil_0 in the interval γ ($\gamma = 165° \pm 22.5°$ electrical angle) to check the optimization effect of the air-gap magnetic field. Several sets of scenarios are listed in Table 3 for different values of L, β, and α, respectively. The no-load back EMF waveforms of the unilateral conductor Coil_0 in interval γ in different schemes and the prototype are shown in Figure 12.

TABLE 3. The values of the concave slots parameters for different scenarios.

	L	β	α
Unit	mm	deg	deg
Scheme 1	2	35	5
Scheme 2	3	35	5
Scheme 3	3	40	5
Scheme 4	2	35	10

By comparing the magnitude of the no-load back-EMF of the unilateral conductor Coil_0 between different schemes, it can be seen that L, β, and α all affect the no-load back EMF. In addition, a concave slot in the magnetic ring causes changes in motor torque and torque ripple. Therefore, the determination of each parameter in the concave slot should not unilaterally consider only the commutation performance but should be considered comprehensively from multiple dimensions. In this optimization, commutation performance, average torque, and torque ripple will be selected as the optimization objectives, and to obtain a non-inferior solution for all three at the same time, a multi-objective optimization of the motor is required.

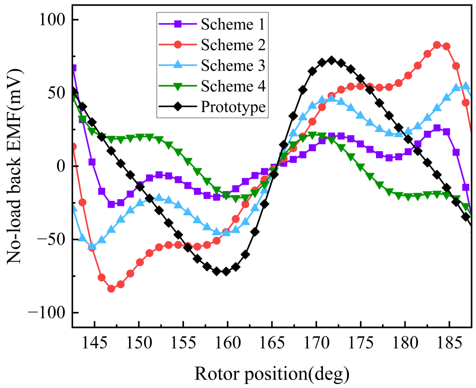

FIGURE 12. The no-load back EMF of the unilateral conductor Coil_0 in the interval γ.

3. PMDCM MULTI-OBJECTIVE OPTIMIZATION

3.1. Optimize the Problem Description

This time, the average torque, torque ripple, and commutation performance are taken as the motor optimization objectives. On the one hand, the motor is required to meet a certain average torque; on the other hand, the motor is required to have a smaller torque ripple and better commutation performance. Taking the concave slots depth L, arc angle β, and edge transition angle α as optimization variables, the specific problem of motor structure optimization can be summarized as formula (15).

$$\begin{cases} f_1 : \max T_{avg} \\ f_2 : \min T_r \\ f_3 : \min F \\ s.t\ 0.5\,\text{mm} \leq L \leq 4.5\,\text{mm} \\ \quad 28° \leq L \leq 42° \\ \quad 0° \leq \alpha \leq 25° \end{cases} \tag{15}$$

where f_1, f_2, f_3 are the three optimization objectives; max and min indicate that the optimization objectives are maximum and minimum; T_{avg} denotes the average value of torque; T_r denotes the torque ripple; and F denotes the amplitude of the no-load back EMF of the unilateral conductor Coil_0 in the interval γ.

3.2. Analysis of PSO Algorithm and Optimization Results

PSO algorithm is a kind of optimization algorithm based on population evolution theory [22], which has the advantages of simple calculation, few adjustable parameters, fast convergence speed, and strong robustness, and its optimization flow is shown in Figure 13. The basic equation of PSO algorithm can be expressed by formula (16).

$$\begin{cases} V_{id}^{k+1} = \omega V_{id}^{k} + c_1 r_1 \left(P_{id}^{k} - X_{id}^{k}\right) + c_2 r_2 \left(Q_{id}^{k} - X_{id}^{k}\right) \\ X_{id}^{k+1} = X_{id}^{k} + V_{id}^{k+1} \end{cases} \tag{16}$$

where V_{id} and X_{id} are the velocity and position of the ith particle in d-dimensional space, respectively; k, d, and ω represent the number of iterations, the size of the particle search space,

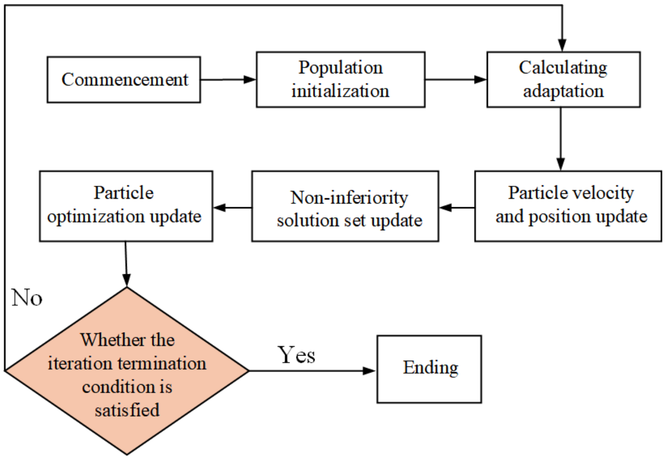

FIGURE 13. Particle swarm optimization (PSO) algorithm flow.

and the inertial weight, respectively; r_1 and r_2 are random numbers between [0, 1]; c_1 and c_2 represent the acceleration coefficients; Q and P represent the global optimum and local optimum, respectively

To enhance the optimization of the initial global search and ensure that the particles converge to the global optimum solution in later stages of the search, the inertia weight coefficient ω in the above equation is set to decrease linearly from $\omega_{\max} = 0.9$ to $\omega_{\max} = 0.2$, as shown in formula (17). The acceleration coefficients c_1 and c_2 are set to use an asynchronous time-varying method, as shown in formula (18).

$$\omega = \omega_{\max} - (\omega_{\max} - \omega_{\min}) \frac{k}{Nc_{\max}} \tag{17}$$

$$\begin{cases} c_1 = c_{1\max} - (c_{1\max} - c_{1\min}) \frac{k}{Nc_{\max}} \\ c_2 = c_{2\max} + (c_{2\max} - c_{2\min}) \frac{k}{Nc_{\max}} \end{cases} \tag{18}$$

The prerequisite for multi-objective optimization of the motor is to establish a parametric model of the variables. Before simulation, a parametric model of the magnetic ring should be established in Maxwell 2D using the concave slots depth L, arc angle β, and edge transition angle α as parametric variables. This paper is based on OptSLang and combines PSO algorithm to perform sensitivity analysis on the schemes. The optimization results are presented in the form of a Pareto 3D optimal solution set, as shown in Figure 14.

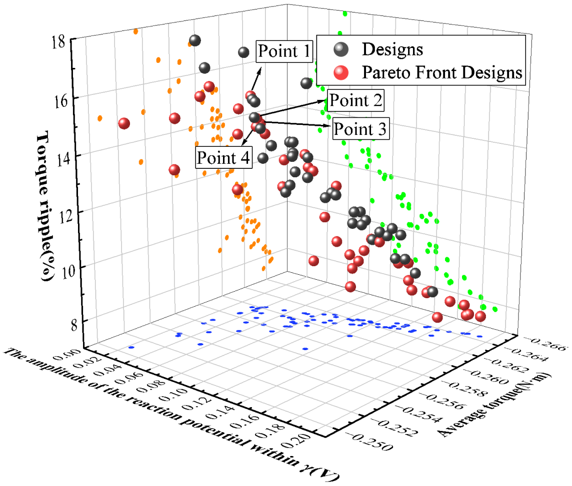

FIGURE 14. The multi-objective optimization of optimal solution sets (Pareto 3D).

TABLE 4. The comparison of the optimization results for different optimization schemes.

	T_{avg}	T_r	F
Unit	mN·m	%	mV
Point 1	259.7	15.23	33.02
Point 2	259.8	14.4	29.47
Point 3	260.1	14.2	30.33
Point 4	259.7	14.11	37.77

From Figure 14, the coordinate axes in the figure represent the average torque, torque ripple, and no-load back EMF of the unilateral conductor Coil_0 in the interval γ, respectively. The points in the figure represent particles with different input variables. Black represents particles that do not meet the constraint conditions, while red represents particles that meet the constraint conditions. The optimal solution set of the scheme is located on the Pareto front. it can be seen that the optimization scheme is more effective in optimizing the torque ripple, but due to the reduction in the amount of permanent magnets, it leads to a decrease in the average torque. This optimization requires that the average motor torque $T_{avg} \geq 259$mN·m and no-load back EMF amplitude $F \leq 40$ mV for the unilateral conductor Coil_0 in the interval γ. According to the requirements, four more optimal schemes can be selected from them, i.e., Points 1 to 4. The optimization results of the four scenarios are shown in Table 4.

From Table 4, it can be seen that the simulation results of the four schemes are relatively close to each other, and the cogging torque amplitude T_{cog} can be further analyzed to select the final optimization scheme from them. The cogging torques of the four schemes and the prototype are shown in Figure 15.

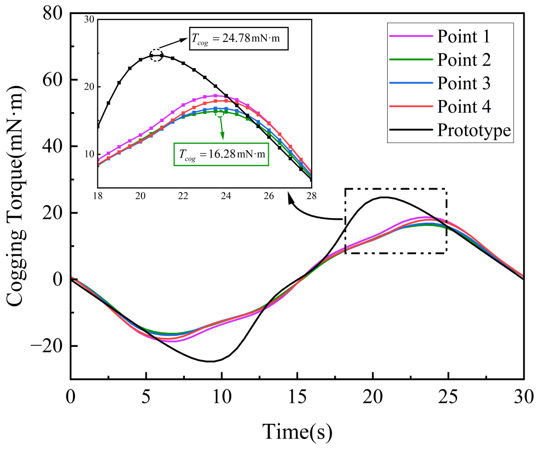

FIGURE 15. The cogging torques of the different schemes with the prototype.

The simulation results show that T_{cog} of the four optimized schemes are lower than that of the prototype. The cogging torque magnitude of the prototype is 24.78 mN·m, and the cogging torque magnitude of Point 2 is 16.28 mN·m. Here, Point 2 ($L = 2.4$ mm, $\beta = 34.02°$, $\alpha = 11°$) is selected as the final optimized scheme. The optimized motor structure is shown in Figure 16.

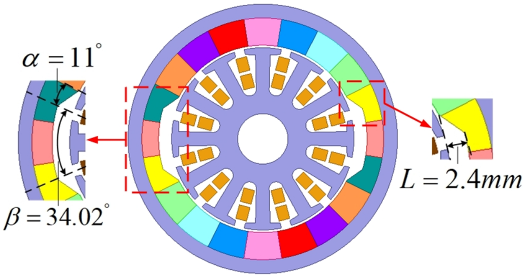

FIGURE 16. The final optimized structure of the CSHAMR.

3.3. Motor Performance Comparison before and after Optimization

The no-load back EMF waveforms of the before and after optimization unilateral conductor Coil_0 in the interval γ are shown in Figure 17, and the radial air-gap magnetic flux density waveform is shown in Figure 18. The amplitude of the no-load back EMF of the optimized unilateral conductor Coil_0 in the interval γ is reduced from 72.2 mV to 29.47 mV, a reduction of 59.18%. The magnetic field strength in the commutation interval is significantly lower than that before slotting (THAMR).

The optimized magnetic flux density distribution of the motor is shown in Figure 19. The magnetic flux density on both sides of the machine housing has been significantly reduced compared to the prototype, which can improve the local magnetic saturation problem caused by the machine housing being too thin.

The motor torque curves before and after optimization are shown in Figure 20, and the cogging torque is shown in Figure 21. The average torque of the motor decreases slightly after optimization, but the optimization of torque ripple and cogging torque is more obvious. The torque ripple decreases from 23.12% to 14.4%, and the cogging torque amplitude decreases from 24.78 mN·m to 16.28 mN·m, a decrease of 34.3%. A summary of the optimized performance parameters of the motor is shown in Table 5, where F is the no-load back EMF amplitude of the unilateral conductor Coil_0 in the interval γ.

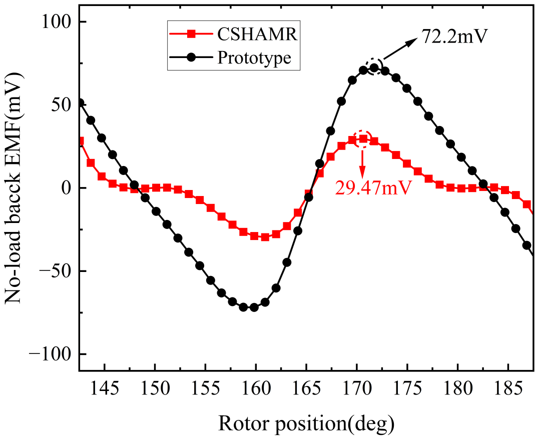

FIGURE 17. The no-load back EMF of the unilateral conductor Coil_0 in the interval γ.

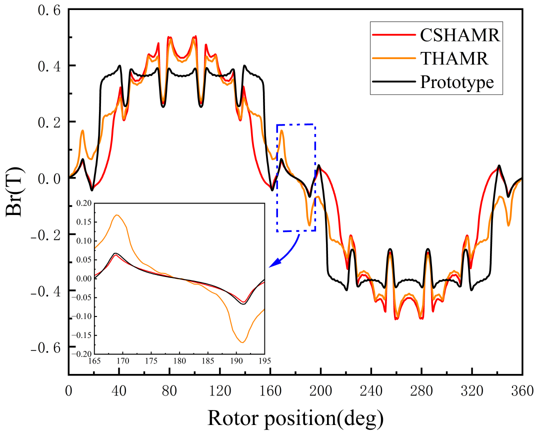

FIGURE 18. The radial air-gap magnetic flux density between different schemes.

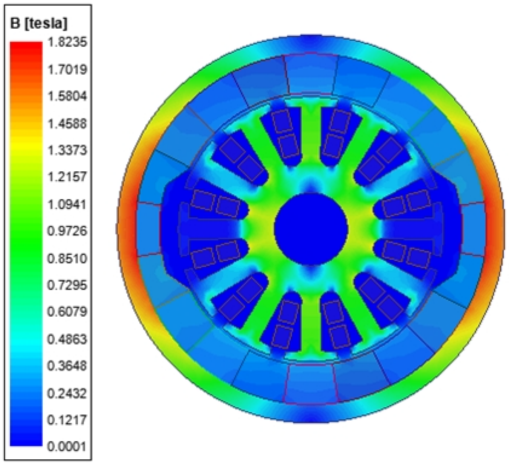

FIGURE 19. The magnetic flux density distribution of the CSHAMR scheme.

TABLE 5. The summary of the PMDCM performance parameters before and after optimization.

	T_{avg}	T_r	T_{cog}	F
Unit	mN·m	%	mN·m	mV
Prototype	263.5	23.12	24.78	72.2
CSHAMR	259.8	14.4	16.28	29.47
$\varepsilon_{\text{CSHAMR}}$ (%)	−1.4%	−37.72%	−34.3%	−59.18%

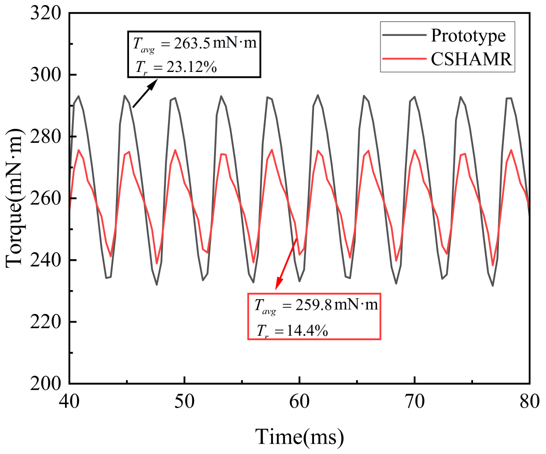

FIGURE 20. The torque curve before and after optimization.

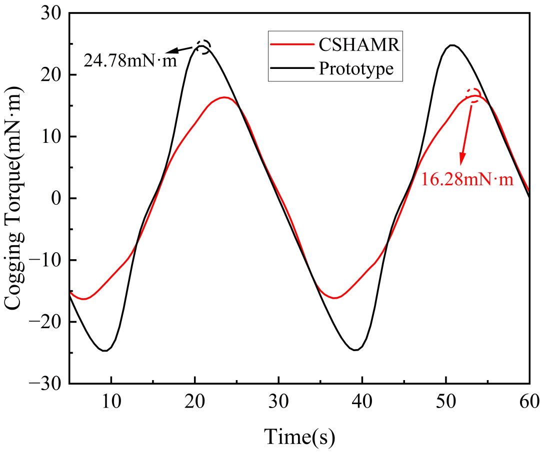

FIGURE 21. The cogging torque curves before and after optimization.

4. CONCLUSION

In this paper, a 2-pole, 12-slot PMDCM has been optimized using a Halbach array, and the CSHAMR structure has effectively reduced the air-gap magnetic field strength in the commutation interval. A parametric model of the CSHAMR was established and combined with PSO algorithm for multi-objective optimization of the motor, which yielded the following results

(1) The air-gap magnetic field strength in the commutation interval is significantly reduced in CSHAMR compared to THAMR. The amplitude of the no-load back EMF of the unilateral conductor Coil_0 in the interval γ decreases by 59.18% compared to the prototype, and the commutation performance has been optimized to some extent.

(2) The air-gap magnetic field waveform of the prototype is an approximate trapezoidal waveform, and CSHAMR is an approximate sinusoidal waveform. Although the average motor torque is slightly decreased after optimization, the optimization of torque ripple and cogging torque is more obvious, which are reduced by 37.72% and 34.3%, respectively.

(3) The magnetic ring structure can effectively improve the problem of local magnetic saturation on both sides of the machine housing caused by the prototype machine housing being too thin.

Based on the above conclusions, it can be seen that CSHAMR effectively improves the problem of the increased air-gap magnetic field in the commutation interval caused by the use of the THAMR. In addition, the approximate sinusoidal wave air-gap magnetic field formed by the Halbach array can optimize the motor torque ripple and cogging torque, which is conducive to the improvement of the stability of the motor operation and the reduction of the operation noise. The design of this paper can provide some reference value for the application of the Halbach array in brushed DC motors.

REFERENCES

[1] Zhang, J., J. Wang, and J. Liu, "Modeling and prediction of electromagnetic interference for brushed DC motors," *Tongji Univ. (Nat. Sci.)*, Vol. 50, No. S1, 237–246, 2022.

[2] Ilka, R., Y. Alinejad-Beromi, and H. Yaghobi, "Cogging torque reduction of permanent magnet synchronous motor using multi-objective optimization," *Mathematics and Computers in Simulation*, Vol. 153, 83–95, 2018.

[3] Shin, K.-H., H.-I. Park, H.-W. Cho, and J.-Y. Choi, "Analytical calculation and experimental verification of cogging torque and optimal point in permanent magnet synchronous motors," *IEEE Transactions on Magnetics*, Vol. 53, No. 6, 1–4, 2017.

[4] Halbach, K., "Design of permanent magnet multipole magnets with oriented rare earth cobalt material," *Nucl. Instrum. Methods*, Vol. 169, No. 1, 1–10, 1980.

[5] Zhang, Y., Q. Liu, Y. Lei, J. Cao, and W.-H. Liao, "Circular Halbach negative stiffness isolating from torsional vibration: Design, modeling and experiments," *Mechanical Systems and Signal Processing*, Vol. 202, 110711, 2023.

[6] Ni, Y., K. Chen, B. Xiao, and W. Qian, "Analytical modeling of surface-inset machines having harmonics injected into Halbach magnet shape with salient iron," *International Journal of Applied Electromagnetics and Mechanics*, Vol. 71, No. 3, 287–303, 2023.

[7] Trang, H., A. Castellazzi, S. Domae, T. Dong, and T. Nakamura, "Light electric vehicle motor-drive design based on hybrid Si/SiC Y-inverter and dual-rotor Halbach machine," *Journal of Electrical Engineering & Technology*, Vol. 18, No. 1, 367–376, 2023.

[8] Pérez, R., A. Pelletier, J.-M. Grenier, J. Cros, D. Rancourt, and R. Freer, "Comparison between space mapping and direct FEA optimizations for the design of Halbach array PM motor," *Energies*, Vol. 15, No. 11, 3969, 2022.

[9] Cheng, H., X. Tang, Z. Ma, *et al.*, "Tooth groove torque weakening of asynchronous starting permanent magnet synchronous motor," *Journal of Harbin University of Science and Technology*, 1–8.

[10] Yang, Z., Y. Zhang, Z. Wu, *et al.*, "Mathematical model and minimization method of speed harmonics caused by pmsm groove torque," *Electric Machines and Control*, Vol. 27, No. 03, 30–41, 2023.

[11] Tymosch, T., M. Fischer, V. Ketchedjian, Y. Terao, and H. Ohsaki, "Analysis of superconducting synchronous motors with Halbach array field excitation," *IEEE Transactions on Applied Superconductivity*, Vol. 31, No. 2, 1–5, 2021.

[12] Shen, Y. and Z. Q. Zhu, "Investigation of permanent magnet brushless machines having unequal-magnet height pole," *IEEE*

Transactions on Magnetics, Vol. 48, No. 12, 4815–4830, Dec. 2012.

[13] Kou, B., H. Cao, W. Li, and X. Zhang, "Analytical analysis of a novel double layer Halbach permanent magnet array," *Transactions of China Electrotechnical Society*, Vol. 30, No. 10, 68–76, 2015.

[14] Zhang, L., B. Kou, F. Xing, and B. Zhao, "Characteristic analysis of an ironless linear synchronous motor with novel halbach magnet array," in *2014 17th International Symposium on Electromagnetic Launch Technology*, 1–5, La Jolla, CA, USA, Jul. 2014.

[15] Zhang, L. and B. Kou, "Investigation of a novel 2-D Halbach magnet array for magnetically levitated planar motor," in *2017 20th International Conference on Electrical Machines and Systems (ICEMS)*, 1–5, Sydney, NSW, Australia, Aug. 2017.

[16] Zhang, X., C. Zhang, J. Yu, P. Du, and L. Li, "Analytical model of magnetic field of a permanent magnet synchronous motor with a trapezoidal Halbach permanent magnet array," *IEEE Transactions on Magnetics*, Vol. 55, No. 7, 1–5, Jul. 2019.

[17] Shi, T., Z. Qiao, C. Xia, H. Li, and Z. Song, "Modeling, analyzing, and parameter design of the magnetic field of a segmented Halbach cylinder," *IEEE Transactions on Magnetics*, Vol. 48, No. 5, 1890–1898, 2012.

[18] Lv, P., H. Ma, X. Su, D. Xu, Z. Liu, and L. Liu, "Multi-objective optimization of permanent magnet motor based on Improved Salp Swarm Algorithm and Spearman correlation," *International Journal of Applied Electromagnetics and Mechanics*, Vol. 75, No. 4, 459–477, 2024.

[19] Li, L., G. Wang, C. Tan, Z. Sun, H. Xu, and Z. Lu, "Design and optimization of Halbach-eccentric pole permanent magnet synchronous motor," *Shandong Univ. Technol. (Nat. Sci. Ed.)*, Vol. 37, No. 6, 56–62, 2023.

[20] Zhu, Z. Q., Z. P. Xia, K. Atallah, G. W. Jewell, and D. Howe, "Novel permanent magnet machines using Halbach cylinders," in *Proceedings IPEMC 2000. Third International Power Electronics and Motion Control Conference (IEEE Cat. No.00EX435)*, Vol. 2, 903–908, Beijing, China, 2000.

[21] Zhu, Z., "A study on improving the performance of pole change of high-speed direct-current motor," *Jiangsu Teach. Univ. Technol.*, Vol. 8, No. 4, 12–14, 2002.

[22] Xue, F., "Electromagnetic design and torque performance optimization of double V built-in permanent magnet synchronous motor for vehicle," Master's thesis, Shanghai DianJi University, Shanghai, 2023.